nature communications

Article

https://doi.org/10.1038/s41467-024-55265-z

Structure-function analysis of carrier protein-dependent 2-sulfamoylacetyl transferase in the biosynthesis of altemicidin

Received: 5 July 2024

Accepted: 4 December 2024

Yuhao Zhu[1], **Takahiro Mori**[1,2,3], **Masayuki Karasawa**[4], **Kohei Shirai**[1], **Wenjiao Cheng**[1], **Tohru Terada**[4], **Takayoshi Awakawa**[1,5] **& Ikuro Abe**[1,2]

The general control non-repressible 5 (GCN5)-related *N*-acetyltransferase (GNAT) SbzI, in the biosynthesis of the sulfonamide antibiotic altemicidin, catalyzes the transfer of the 2-sulfamoylacetyl (2-SA) moiety onto 6-azatetrahydroindane dinucleotide. While most GNAT superfamily utilize acyl-coenzyme A (acyl-CoA) as substrates, SbzI recognizes a carrier-protein (CP)-tethered 2-SA substrate. Moreover, SbzI is the only naturally occurring enzyme that catalyzes the direct incorporation of sulfonamide, a valuable pharmacophore in medicinal chemistry. Here, we present the structure-function analysis and structure-based engineering of SbzI. The crystal structure of SbzI in complex with the CP SbzG, along with cross-linking and isothermal titration calorimetry analyses of their variants, revealed the structural basis for CP recognition by the GNAT SbzI. Furthermore, docking simulation, molecular dynamics simulation, and mutagenesis studies indicated the intimate structural details of the unique reaction mechanism of SbzI, which does not utilize a general base residue in contrast to other typical GNATs. These findings facilitated rational engineering of the enzyme to expand the substrate range and to generate azaindane dinucleotide derivatives.

The General Control Non-repressible 5 (Gcn5)-related *N*-acetyltransferases (GNAT) superfamily enzymes catalyze the transfer of acyl groups of varying lengths, ranging from C_1 to C_{32}, from an acyl-coenzyme A (acyl-CoA) onto the amino group of acyl acceptors, including small molecules and proteins[1]. These enzymes are widely distributed across archaea, bacteria, and eukaryotes[2], and play crucial roles in various biological processes such as gene expression regulation[3–6], metabolic pathway control[7–10], antibiotic resistance development[11–17], stress response[18–20], infection resistance[21], detoxification[22–26] and anti-oxidation[27,28]. The GNAT superfamily enzymes also participate in the biosynthesis of secondary metabolites, such as polyketides (PK)[29–31], PK/nonribosomally-synthesized peptides (PK/NRP) hybrid lipopeptides[32–37], and ribosomally-synthesized and post-translationally modified peptides (RiPPs) lipopeptides[38].

While the majority of GNAT superfamily members utilize acyl-CoA as a substrate, notable exceptions are the acyl-carrier protein (acyl-CP)-dependent GNAT enzymes, such as GdvG/AprG in goadviolin biosynthesis[39], GNAT-like decarboxylases[30,40–42], and the *N*-acyl amino acid synthase FeeM[43]. To date, over 500 crystal structures of CoA-accepting GNATs have been characterized. However, only a few structures of CP-dependent GNATs, including GphF[40] and CurA[41], and the *N*-acyl amino acid synthase FeeM[43] have been solved, but not in complex with CP. Moreover, due to the low sequence similarity among

---

[1]Graduate School of Pharmaceutical Sciences, The University of Tokyo, Tokyo, Japan. [2]Collaborative Research Institute for Innovative Microbiology, The University of Tokyo, Tokyo, Japan. [3]FOREST, Japan Science and Technology Agency, Saitama, Japan. [4]Graduate School of Agricultural and Life Sciences, The University of Tokyo, Tokyo, Japan. [5]RIKEN Center for Sustainable Resource Science, Wako, Saitama, Japan. e-mail: tmori@mol.f.u-tokyo.ac.jp; takayoshi.awakawa@riken.jp; abei@mol.f.u-tokyo.ac.jp

acyl-CP-dependent GNATs, the interactions between GNATs and CP, and particularly how GNAT enzymes recognize CP over CoA substrates, remain unclear.

Altemicidin is a sulfonamide antibiotic originally isolated from *Streptomyces sioyaensis* SA-1758, with promising antitumor activity (Fig. 1A)[44]. We previously identified the biosynthetic gene cluster (*sbz* cluster) for altemicidin and its analogs from *Streptomyces* sp. NCIMB 40513[45,46]. In the biosynthetic pathway, the sulfonamide moiety is incorporated by a key GNAT, SbzI. While GNAT superfamily enzymes usually accept fatty acyl-CoAs as substrates, the CP-dependent SbzI uniquely recognizes sulfonamide as a donor substrate. 2-Sulfamoylacetic acid (2-SA), derived from L-Cys, is first enzymatically activated by the adenylation enzyme SbzL to form 2-SA-AMP. SbzL then transfers 2-SA-AMP onto the 4′-phosphopantetheine (Ppant) arm of the acyl-CP SbzG. Subsequently, the 2-SA group is installed onto the amino group of 6-azatetrahydroindane dinucleotide **1** by the GNAT enzyme SbzI (Fig. 1A). The lower basicity and greater structural rigidity of the sulfonamide contribute to diverse biological activities, making it a valuable pharmacophore in medicinal chemistry. However, its incorporation into natural products is rare, and the mechanism of sulfonamide introduction remains largely unknown. SbzI is the only naturally occurring enzyme that catalyzes the direct incorporation of sulfonamide in natural product biosynthesis. Therefore, the molecular mechanism by which the enzyme recognizes sulfonamides has attracted keen interest.

Previous in vitro assays revealed that SbzI exhibits high substrate specificity for **1**. While SbzI efficiently converts **1** to **2**, its reactivities with **3** and **4** are less than 10% compared to that with **1**. In addition, compounds **5** and **6**, lacking the C2 hydroxyl group, were not accepted as substrates (Fig. 1B)[46]. These observations indicated that SbzI strictly recognizes the dinucleotide moiety derived from β-NAD and the C2-hydroxy group of the azaindane scaffold. The structural basis for the recognition of the 2-SA, 6-azatetrahydroindane dinucleotide **1**, and CP SbzG, as well as the mechanism of the 2-SA transfer reaction catalyzed by SbzI, remains to be elucidated.

In this work, we investigate the reaction mechanism of SbzI and the protein-protein interactions between SbzI and SbzG, using X-ray crystallography, cross-linking reactions, isothermal titration calorimetry (ITC) analysis, and structure-based mutagenesis experiments. The complex structure of SbzI with SbzG reveals that SbzI recognizes SbzG primarily through hydrophobic interactions, supported by salt bridges and hydrogen bonds. Comparisons of the structure of SbzI with those of other CP-dependent GNATs suggest that similar recognition mechanisms are shared by these enzymes for donor substrate installation. Moreover, the model structure of SbzI with compound **1** and subsequent mutagenesis studies suggest that SbzI does not utilize a general base residue for the reaction, in contrast to other typical GNAT enzymes employing acid/base catalysis. Finally, we also successfully expand the substrate scope through structure-based rational protein engineering.

Results

Crystal structure of SbzI

To understand the structural basis of the enzyme reaction, we crystallized SbzI and solved the structure at 2.5 Å resolution (Supplementary Fig. S1A and Supplementary Table S1). The overall structure of SbzI consists of six β-strands and four α-helices and is similar to those of classic GNATs, including *Tv*Alba *N*-acetyltransferase Ard1[47] from *Thermoplasma volcanium* (PDBID: 4PV6, 13% amino acid (AA) sequence identity) and ribosomal protein S18 *N*-acetyltransferase RimI[48] from *Salmonella typhimurium* LT2 (PDBID: 2CNT, 16% AA sequence identity), with RMSD values of 1.9 and 2.0 Å for Cα-atoms, respectively (Supplementary Fig. S1B, C). The structure is also similar to that of the CP-dependent N-acyl amino acid synthase FeeM[43], with an RMSD value of 2.5 Å for Cα-atoms and 12% AA sequence identity (Supplementary Fig. S1D). Structural comparisons of SbzI with these enzymes revealed that the second alpha-helix (α2) is extended by three residues, and the loop between α2 and α3, involved in the formation of part of the active site, is longer than those of Ard1 and RimI. At the acyl donor binding site, the loop between α5 and the sixth beta-sheet (β6)

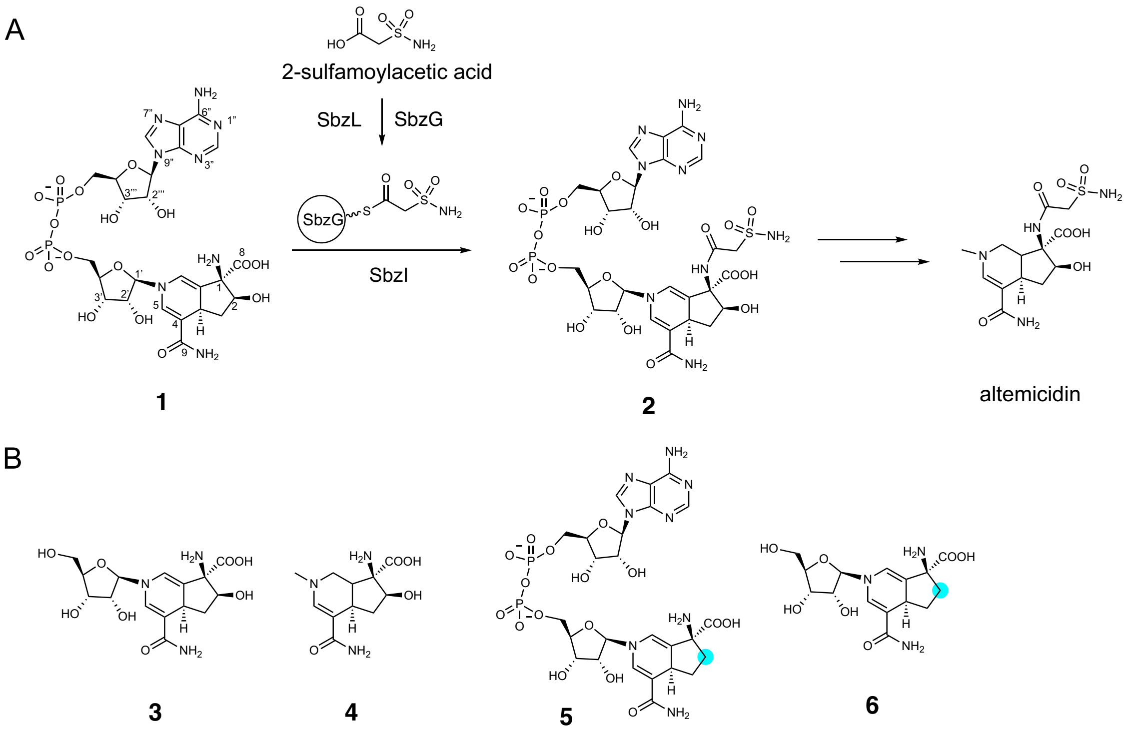

Fig. 1 | Enzyme reaction of SbzI. A Reaction catalyzed by SbzI. **B** Substrate analogs of substrate 1 tested previously. The reactivities of SbzI with 3 and 4 are less than 10% compared to that with 1. Compounds 5 and 6, lacking the C2 hydroxyl group, were not accepted by SbzI.

in SbzI exhibited considerable differences in length and conformation compared to that of FeeM (β6 and β7). As a result, SbzI has a deep cleft that is large enough to accommodate compound **1** (Supplementary Fig. S2). Furthermore, due to the substitutions of the P-loop residues (Gln/Arg-x-x-Gly-x-Gly/Ala), which are crucial for interactions with the diphosphate and adenine moieties of CoA in acyl-CoA-accepting GNATs[49], with 111GGSLVGL117 in SbzI, a substantial conformational difference of the loop was observed. In the SbzI structure, three different conformations of P-loop-like region were observed among six monomers in the asymmetric unit (conformation A in monomers A/C, conformation B in monomers B/D, and disordered in monomers E/F), suggesting the flexibility of P-loop like region (Supplementary Fig. S3A–D). None of these conformations is similar to those of Ard1 or RimI (Supplementary Fig. S3E–G). In conformation A, the P-loop-like region is positioned near the Ppant arm-binding tunnel, whereas in conformation B, it shifts 4.5 Å to the opposite side of the tunnel. These distinctive sequential and conformational changes in the P-loop were also observed in FeeM, suggesting that they are characteristic features of CP-dependent GNAT enzymes[43]. The substitution of the P-loop-like region of SbzI with those of Ard1 (RRMGVG) or RimI (RGLGRM) resulted in a significant decrease in activity, to 2% and 5%, respectively, compared to the wild-type SbzI (Supplementary Fig. S4). This result indicated that the special P-loop region of SbzI is crucial for the recognition of the CP-attached Ppant arm.

Elucidation of the interaction between SbzI and SbzG

To elucidate how SbzI selectively recognizes CP during the reaction, we solved the structure of the SbzI/SbzG complex. Due to the weak interactions between SbzI and SbzG (Supplementary Fig. S5 and Supplementary Table S3), we used ColabFold to design an SbzI and SbzG fusion protein and facilitate the formation of the SbzI/SbzG complex crystals. The complex model of SbzGI suggested the proximity between the C-terminus of SbzG and the N-terminus of SbzI (Supplementary Fig. S6A). Therefore, a short, flexible Gly-Gly-Gly-Gly-Ser (GGGGS) linker was introduced between the C-terminus of SbzG and the N-terminus of SbzI to construct the SbzG-SbzI fusion protein (SbzGI)[50] (Supplementary Fig. S6B). In vitro assays of the SbzGI fusion enzyme revealed that its activity was increased by around 3-fold, compared to the individual reactions of SbzI and SbzG (Supplementary Fig. S6C).

The crystal structure of holo-SbzGI (modified with the Ppant arm at Ser38 of SbzG (Ser38$_G$)) was successfully solved at 2.6 Å resolution (Fig. 2A and Supplementary Fig. S6D). A comparison of the SbzI and SbzGI structures revealed no significant overall conformational changes of SbzI upon CP binding and Ppant arm insertion into the active site of SbzI (RMSD value of 0.6 Å for Cα-atoms) (Supplementary Fig. S7).

However, the conformation of the P-loop-like region of SbzGI is slightly different from that of the SbzI structure. Two conformations (conformation C and D) of the P-loop-like region, which are different from those in SbzI structures, were observed in monomer A. In conformation C, the P-loop-like region covers the entrance of the Ppant binding tunnel, and the main chain carbonyl of Gly111$_I$ forms a hydrogen bond with the main chain amide of Ser38$_G$ on α2 of SbzG (Fig. 2). On the other hand, in conformation D, the P-loop-like region moves to the opposite side of α2 of SbzG that opens the entrance of the Ppant binding tunnel more widely.

The phosphate of the Ppant arm interacts with the main chain amide of Leu114$_I$ in both conformations, suggesting that the P-loop-like region plays an important role in binding to CP and the Ppant arm (Fig. 2 and Supplementary Fig. S7). In monomer B, only one conformation was observed, which resembles conformation C but is shifted ~1.5 Å to the opposite side of SbzG (Supplementary Fig. S7). Furthermore, α2 of SbzG and α7 of SbzI are shifted by ~2 Å to the opposite side of the Ppant binding tunnel compared to those in monomer A. Due to the widened entrance of the Ppant binding tunnel, the binding mode of the Ppant arm differs significantly from that in monomer A. The Ppant arm is more deeply embedded in the tunnel in monomer A, suggesting that the binding mode in monomer A represents the active state.

SbzG adopts the typical CP structure composed of four α-helices. The structure is similar to those of other CPs, including the CP-domains of glycine:[carrier protein] ligase from *Bradyrhizobium japonicum* (PDBID: 4H2U)[51] and VinL in the biosynthesis of vicenistatin from *Streptomyces halstedii* (PDBID: 7F2R)[52], with RMSD values of 1.5 and 1.7 Å for Cα-atoms, respectively (Supplementary Fig. S8). The interaction surface between SbzG and SbzI comprises four α-helices: α4 and α5 of SbzI and α2 and α3 of SbzG, which mainly consist of hydrophobic residues, suggesting that SbzI and SbzG interact through hydrophobic interactions (Fig. 2C). In addition, Glu49$_G$ forms a salt bridge with Arg121$_I$ and a hydrogen bond with the main chain of Phe56$_G$, and Glu125$_I$ interacts with the main chain amide of Ala58$_G$ (Fig. 2D).

To verify the importance of these interactions, we performed a mutagenesis analysis (Fig. 2E and S9). First, Glu49$_G$, Arg121$_I$, and Glu125$_I$ were individually substituted with leucine to investigate the importance of salt bridges and hydrogen bonds in the SbzI-SbzG interaction. The SbzGI E49$_G$L, R121$_I$L, and R121$_I$L/E125$_I$L variants decreased the activity to 30, 63, and 74% of the wild type, respectively, while E125$_I$L still maintained comparable activity to the wild type (92%). These results indicated that the electrostatic interaction between Glu49$_G$ and Arg121$_I$ is important for the SbzI-SbzG interaction, while the hydrogen bond at Glu125$_I$ is less critical. Second, to examine the importance of hydrophobic interactions at the SbzGI interface for CP recognition, hydrophobic residues of SbzG, including Val41$_G$, Ala42$_G$, Ile45$_G$, Val46$_G$, Val61$_G$, and Phe66$_G$, were substituted with hydrophilic residues of similar sizes. The SbzGI V41$_G$T, A42$_G$S, I45$_G$T, V46$_G$T, V61$_G$T, and F66$_G$Y variants showed decreased activities (41, 72, 38, 72, 34, and 33% compared to that of wild type, respectively). Val41$_G$, Ile45$_G$, Val61$_G$, and Phe66$_G$ form a hydrophobic pocket at the interface between SbzI and SbzG, and the side chain of Leu114$_I$ is inserted into this pocket, facilitating SbzI-SbzG recognition (Fig. 2C). This is one of the reasons why substitutions of these four residues showed higher impacts compared to the A42$_G$S and V46$_G$T variants (Fig. 2E). Further multiple mutations of these hydrophobic residues, including the VA: V41$_G$T + A42$_G$S, VAI: VA + I45$_G$T, VAIV: VAI + V46$_G$T, VAIVV: VAIV + V61$_G$T, and VAIVVF: VAIVV + F66$_G$Y variants, confirmed their involvement in the recognition of SbzI and SbzG. As the hydrophobic pocket was gradually destroyed by the accumulation of mutations, the variants showed a progressive decrease in activity, ranging from 24% for the VA variant to 3.5% for the VAIVVF variant (Fig. 2E and Supplementary Fig. S9). These results clearly indicated that hydrophobic residues are crucial for the interactions between SbzI and SbzG.

We performed a cross-linking assay to further investigate the interactions between SbzI and SbzG. A bifunctional maleimide reagent, 1,2-bis(maleimido)ethane (BMOE), was used to covalently crosslink SbzI and SbzG between the sulfhydryl group at the terminus of the Ppant arm of SbzG and the cysteine residue in the SbzI active site. Since SbzI and SbzG have three (Cys31$_I$, Cys33$_I$, and Cys119$_I$) and one (Cys80$_G$) cysteine residue, respectively, and the active site of SbzI does not contain a cysteine residue, we constructed the SbzI SSSC (C31$_I$S/C33$_I$S/C119$_I$S/E138$_I$C) and SbzG C80$_G$S variants to prevent non-specific cross-linking reactions. The incubation of the SbzI SSSC variant and the holo-SbzG C80$_G$S variant in the presence of BMOE efficiently afforded the covalent complex (Supplementary Fig. S10). Therefore, we introduced further mutations in the interface residues of SbzI SSSC and SbzG C80$_G$S. All variants were expressed except for E125$_I$L and L114$_I$D of SbzI SSSC. The cross-linking reactions revealed that some of the variants, including SbzI SSSC L117$_I$D, L149$_I$D, I152$_I$T, and L153$_I$D, and SbzG C80$_G$S E49$_G$L, A42$_G$S, V61$_G$T, and F66$_G$Y, showed reduced cross-

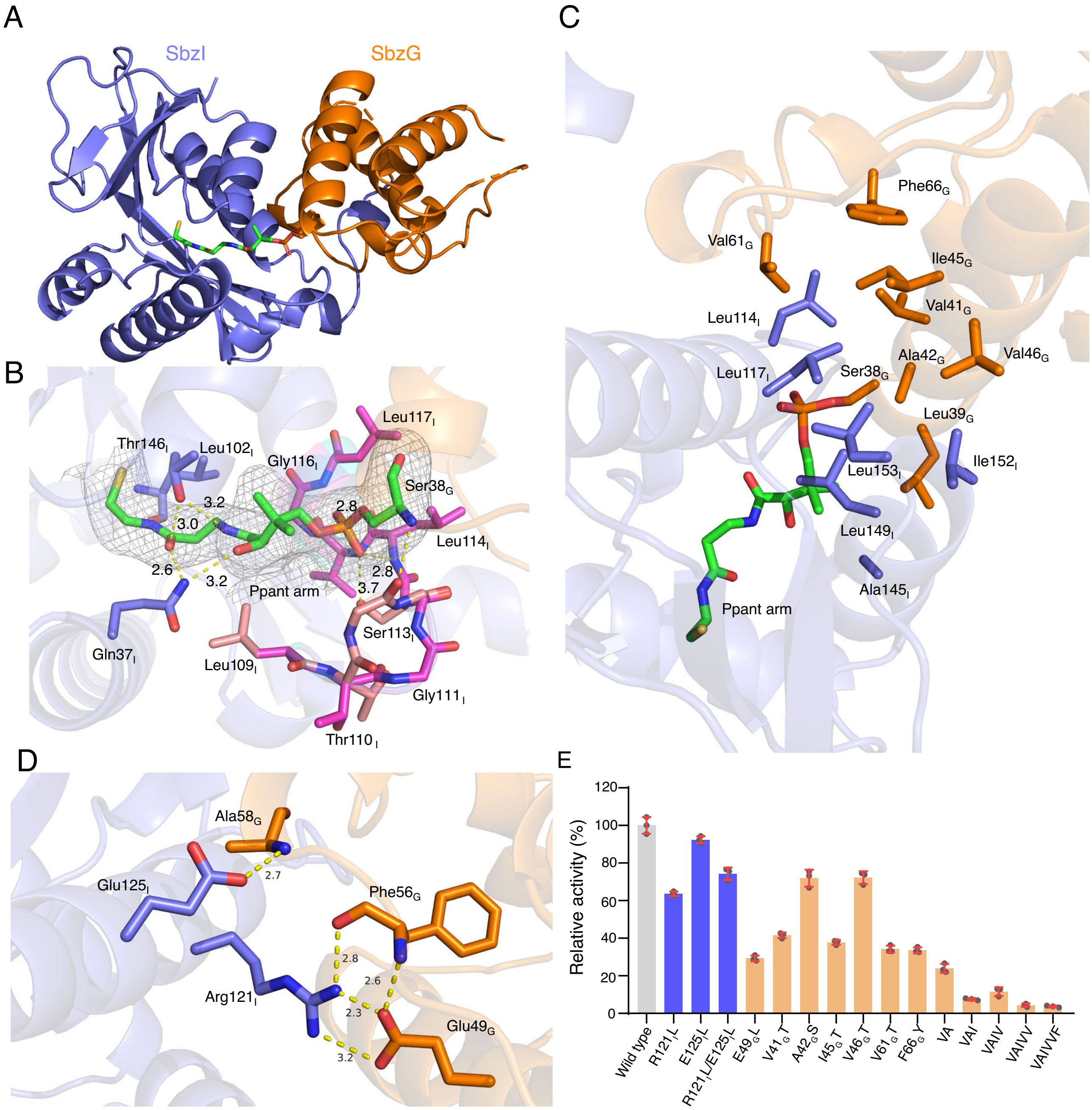

Fig. 2 | Crystal structure of SbzGI fusion protein. A Overall structure of SbzGI. **B** The Ppant arm binding site of SbzI is shown in purple, and the Ppant arm is green. Interactions between the Ppant arm and residues are shown by yellow dashed lines. The Fo-Fc polder map of the Ppant arm (contoured at + 3.0 sigma) is represented by a gray mesh. **C** Hydrophobic interactions at the interface between SbzI and SbzG. **D** Salt bridge and hydrogen bonds (shown by yellow dashed lines) between SbzI and SbzG. **E** Mutagenesis experiment of key residues for investigating the interactions between SbzI and SbzG. The structure and residues of the SbzI part are shown in blue, while those of the SbzG part are shown in orange.

linking efficiency compared to that between SbzI SSSC and SbzG C80$_G$S (Supplementary Fig. S11).

The interaction between SbzI and SbzG was further evaluated by isothermal titration calorimetry (ITC) (Supplementary Fig. S12 and Supplementary Table S3). The wild type of SbzG bound to SbzI with a Ka value of $2.3 \times 10^4 \, M^{-1}$, which is similar to the affinities of other CP-dependent enzymes, such as acyltransferase VinL[52] and malonyl-CoA: acyl carrier protein transacylase HpMCAT[53]. ITC analysis of SbzG variants, including E49$_G$L, V41$_G$T, A42$_G$S, I45$_G$T, V61$_G$T, F66$_G$Y, and multiple hydrophobic residue variants (VAIVV and VAIVVF), revealed a significantly reduced affinity for SbzI. The V41$_G$L and V61$_G$T variants exhibited 28-fold and 2-fold lower Ka values, respectively, and the interactions of the other SbzG variants with SbzI were too weak to accurately determine Ka values. These results are consistent with the results from in vitro assays and cross-linking analysis. These interaction studies highlighted the importance of interface residues in mediating protein-protein interactions between SbzI and SbzG.

Active site architecture of SbzGI complex

The Ppant arm attached to Ser38$_G$ inserts into a 12 Å-long tunnel in SbzI, consisting of helices α2, α4, and α5, a loop between β4 and α4, and a P-loop-like region (Fig. 2B). The position of the Ppant arm is fixed by hydrogen bonds with the residues in the Ppant binding tunnel. The main chain parts of Ser113$_I$, Leu114$_I$, and Gly116$_I$ and the hydroxy group

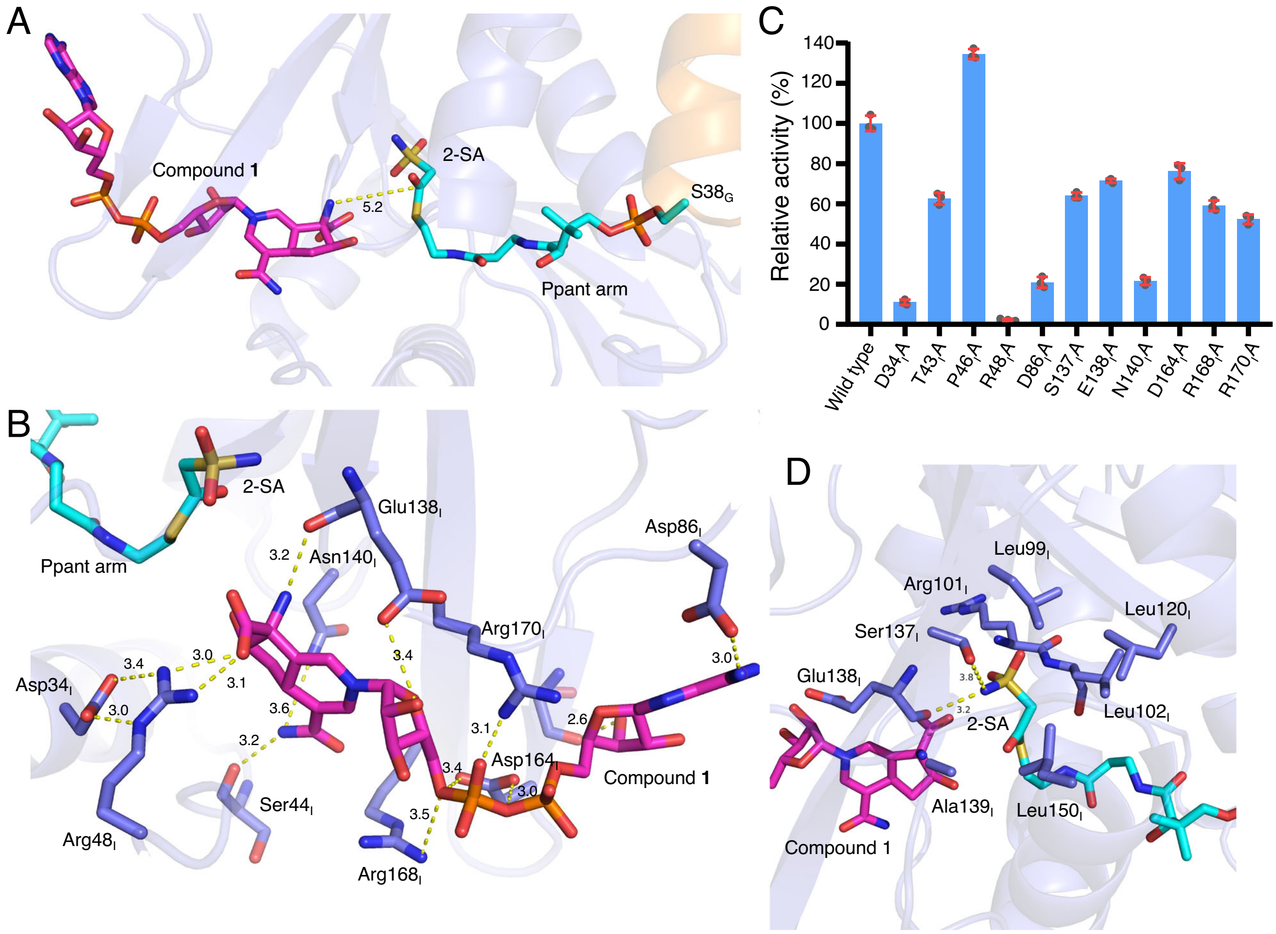

Fig. 3 | Docking model of SbzGI. A Docking model of compound 1 and Ppant arm attached 2-SA, based on the crystal structure of SbzGI. **B** Binding mode of **1** in the active site of SbzGI. Salt bridges and hydrogen bonds are shown by yellow dashed lines. **C** Mutagenesis of active site residues. **D** Binding mode of Ppant attached 2-SA. Structures and residues of the SbzI and SbzG parts are shown in blue and orange, respectively. Compound **1** and Ppant arm attached 2-SA are shown in purple and cyan, respectively.

of Ser113$_{\text{I}}$ form hydrogen bonds with the oxygen atoms in the Ppant arm's phosphate group. Gln37$_{\text{I}}$, Thr146$_{\text{I}}$, and the main chain of Leu102$_{\text{I}}$ interact with the amide carbonyl of the cysteamine moiety and the hydroxy group of the pantothenic acid moiety.

This Ppant binding tunnel guides the sulfhydryl group at the terminus of the Ppant arm into a deep cleft on the opposite surface of SbzI, which is assumed to be the binding site of **1** (Supplementary Fig. S13A). Since attempts to obtain the complex crystal structure of SbzI with compound **1** were unsuccessful, we constructed a docking model with compound **1** and 2-SA-Ppant. In this docking model, compound **1** and the 2-SA moiety bind in the deep cleft of SbzI (Fig. 3A). The residues in the deep cleft interact with compound **1** in the following manners. The C1 carboxyl group of **1** forms a salt bridge network with Arg48$_{\text{I}}$ and Asp34$_{\text{I}}$. The main chain amide carbonyl of Glu138$_{\text{I}}$ forms hydrogen bonds with the C1 amino group. The C4 amide carbonyl group forms a hydrogen bond with Asn140$_{\text{I}}$ and the main chain amide carbonyl of Ser44$_{\text{I}}$. The C2' hydroxy group of the sugar moiety interacts with the side chain carboxyl group of Glu138$_{\text{I}}$, while Asp164$_{\text{I}}$, Arg168$_{\text{I}}$, and Arg170$_{\text{I}}$ interact with the diphosphate moiety of **1**. Furthermore, the main chain of Ser163$_{\text{I}}$ and Asp86$_{\text{I}}$ form a hydrogen bond and a salt bridge with the C2''' hydroxy group of adenosine and the C6'' amine of the adenine moiety, respectively (Fig. 3B).

To validate the docking model, we conducted three independent 1-µs MD simulations (Supplementary Fig. S14). As a result, the binding mode of Ppant-tethered 2-SA remained stable across the three MD runs, with ligand RMSD values averaging 2.8–3.6 Å during the last 400 ns of each run (Supplementary Fig. S14E). The Ppant arm forms hydrogen bonds with residues of SbzI, including the main chain of Leu114$_{\text{I}}$ and the side chain of Thr146$_{\text{I}}$. In the case of compound **1**, distinct fluctuations were observed between the ADP moiety and the azaindane nucleotide moiety. The ADP moiety moved flexibly within the binding site, which led to the high ligand RMSD values, averaging 11.4–14.0 Å across the three MD runs (Supplementary Fig. S14G). The ADP moiety shifted among the loops between β3 and β4, α6 and β6, and α2 and α3 regions, which contain positively charged residues that could form electrostatic interactions with the diphosphate group of the ADP moiety (Supplementary Fig. S15). In contrast, the ligand RMSD values of the azaindane nucleotide moiety were significantly lower than those of the ADP moiety (3.2–6.9 Å, Supplementary Fig. S14H). These observations suggested that the enzyme recognizes both the 6-azatetrahydroindane scaffold and the diphosphate of ADP moiety, and these interactions likely contribute to the dramatic decrease in SbzI reactivity with compounds **3** and **4** compared to **1**[46]. The distances between the nitrogen atom of the C1 amino group of compound **1** and the thioester carbonyl carbon atom of Ppant-tethered 2-SA were maintained during two MD runs, yielding averages of 5.2 Å and 5.9 Å over the last 400 ns, respectively. These distances were consistent with those in the initial docking model (5.2 Å) and were feasible for a nucleophilic attack by the amino group (Fig. 3A). The Cα-RMSD values for the SbzG subunit, SbzI subunit, and the overall structure remained below 3.5 Å, indicating that the docking model was stable (Supplementary Fig. S14B–D).

To evaluate the importance of these residues for substrate recognition, we constructed variants of the binding site of **1**, including SbzGI R48$_I$A, D34$_I$A, D86$_I$A, N140$_I$L, E138$_I$A, D164$_I$A, R168$_I$A, and R170$_I$A, and performed enzyme reactions (Fig. 3C and Supplementary Fig. S16). As a result, SbzGI R48$_I$A and D34$_I$A showed almost no activity (2% and 10% compared with wild type, respectively), indicating that these residues play a key role in fixing the binding position of the amino acid moiety of **1** through the salt bridge network. The SbzGI D86$_I$A and N140$_I$L variants significantly reduced the activity to 21 and 22% of the wild type, respectively, while E138$_I$A, D164$_I$A, R168$_I$A, and R170$_I$A showed moderate impacts on the activity (64, 71, 76, 59, and 52% activities compared with wild type).

The docking model with Ppant-tethered 2-SA also suggested that the sulfonamide moiety is located within a space mainly consisting of Leu99$_I$, Leu102$_I$, Leu120$_I$, Ser137$_I$, Ala139$_I$, and Leu150$_I$. The amino group of sulfonamide interacts with Ser137$_I$ and the main chain carbonyl of Glu138. The main chain amide groups of R101$_I$ and L102$_I$ could form an oxyanion hole near the thioester, which would stabilize the tetrahedral intermediate produced in the general GNAT mechanism[2] (Fig. 3D). The partially hydrophilic environment of this acyl bond space allows SbzI to accommodate the 2-SA moiety, which is likely to be the reason for its unique ability to transfer the sulfonamide.

Expansion of substrate scope by protein engineering

The 2-SA-binding space is large enough to accommodate molecules with carbon chain lengths of four or more atoms, suggesting the catalytic potential for SbzI to accept compounds with fatty acyl chains as substrates. Consequently, we performed a substrate specificity analysis of SbzI towards acyl-donor compounds. The Ser38$_G$ residue of SbzGI was modified with various acyl-CoAs, including C_2-, C_4-, C_6-, C_8-, C_{10}-,C_{12}- and C_{18}-fatty acyl CoAs, malonyl-CoA, methylmalonyl-CoA, succinyl-CoA, prolyl-CoA, and alanyl-CoA, by the promiscuous 4′-phosphopantetheinyl transferase Sfp[54] and the resulting acylated SbzGIs were used for the enzyme reaction (Fig. 4 and Supplementary Fig. S17A). LC-MS/MS analysis of the enzyme reaction products revealed that SbzGI accepts fatty acyl-CPs C_2-,C_4- and C_6-fatty acyl-SbzGs as acyl donors to yield the unnatural **1**-analog compounds **7**, **8**, and **9** (Supplementary Fig. S18A–F). In contrast, long acyl substrates C_8-, C_{10}-, C_{12}-, and C_{18}-fatty acyl-SbzG, as well as hydrophilic substrates, including malonyl-SbzG, methylmalonyl-SbzG, and succinyl-SbzG, were not accepted (Fig. 4B, D). Furthermore, aminoacyl-CPs, alanyl-SbzG, and prolyl-SbzG were also accepted by SbzI to yield compounds **17** and **18**, albeit with low efficiency (Supplementary Fig. S17B).

Since the side chain of Ser137$_I$ interacts with the amino group of the sulfonamide moiety, the function of Ser137$_I$ was further verified by comparing its activity with 2-SA-SbzG and C_6-fatty acyl-SbzG. The SbzGI S137$_I$A variant exhibited 44% activity with 2-SA-SbzG compared to the wild type, while the activity with C_6-fatty acyl-SbzG as a substrate was maintained, suggesting that Ser137$_I$ is involved in the recognition of the sulfonamide moiety (Supplementary Fig. S19).

A comparison of the acyl-binding sites between SbzI and FeeM, which accepts a C_{12} acyl-CP, suggested that Leu99$_I$, Leu120$_I$, and Leu150$_I$ form the bottom surface of the space and restrict the length of the acyl donor accepted by SbzI (Supplementary Fig. S20A, B). To broaden the substrate scope of SbzI, these residues were substituted with alanine. Interestingly, the L150$_I$A variant newly accepted C_8- and C_{10}-fatty acyl-SbzG as substrates, in addition to C_2-, C_4- and C_6-fatty acyl-SbzG, to produce compounds **10** and **11** (Fig. 4C, D and Supplementary Fig. S18G, H). The ColabFold model of SbzGI L150$_I$A confirmed an expanded pocket compared to that of the wild type (Supplementary Fig. S20C). To further expand the substrate scope, the double variants SbzGI L99$_I$A/L150$_I$A, L120$_I$A/L150$_I$A, and S137$_I$A/L150$_I$A were constructed. As expected, these double variants newly accepted C_{12}-fatty acyl-SbzG to generate compound **12** (Fig. 4E, S18I and S21A). The L120$_I$A/L150$_I$A variants still maintained activities toward 2SA-SbzG comparable to that of the wild type, while the L99$_I$A/L150$_I$A and S137$_I$A/L150$_I$A variants showed reduced activities (Supplementary Fig. S21B, C).

Discussion

CP-dependent enzymes, such as fatty acid synthases, PKSs, NRPSs, and amide bond synthases, play crucial roles in the biosynthesis of natural products. Each enzyme precisely recognizes its respective partner CP through distinct interactions[55]. For instance, in the condensation domain of NRPS enzymes, the CP domains of both the peptide donor and acceptor are recognized through hydrophilic and hydrophobic interactions at the front and back of the V-shaped active site tunnel, while the amide bond synthase CcbD, in the biosynthesis of lincosamides, mainly interacts with its CP CcbZ via salt bridges and hydrogen bonds[56]. SbzI and SbzG primarily interact through hydrophobic interactions, specifically between α4 and α5 of SbzI and α2 of SbzG. Their mutual recognition is further supported by a salt bridge and hydrogen bonds between α4 of SbzI and α2 of SbzG. Structural and mutagenesis studies of FeeM suggested the importance of Phe148 and His145 in the interaction with CP FeeL (Supplementary Fig. S22)[43]. Phe148 of FeeM, positioned on an α-helix corresponding to α5 of SbzI, is thought to be involved in hydrophobic interactions with its CP, in a similar manner to SbzI. In contrast, His145 in FeeM, corresponding to Thr146$_I$, forms part of the Ppant tunnel, suggesting that His145 participates in the Ppant interaction rather than FeeL recognition. A comparison of SbzI with other CP-dependent GNATs indicated that hydrophobic residues are located on the α4 and α5 regions of FeeM[43] and CurA[41], suggesting that the recognition mechanism is similar to that of SbzI (Supplementary Fig. S22). In contrast, the residues at these positions in CoA-utilizing GNATs, such as Ard1 and RimI are mainly hydrophilic and important for interactions with the adenine moiety of CoA. These differences in the conservation of amino acid residues in α4 and α5 would be critical for the recognition of CoA or CP by GNAT enzymes.

Our previous in vitro analysis of SbzI revealed that another CP, SbzK, in the *sbz* gene cluster, can serve as a partner protein of SbzI for the sulfonamide transfer reaction[45]. SbzK shares moderate sequence identity (31%) with SbzG. The ColabFold2 model structure suggested that SbzK adopts a similar overall structure to SbzG, and the residues on α3 of SbzK are also conserved as hydrophobic residues. The hydrophobic residues on α3 (Val41$_G$, Ala42$_G$, Ile45$_G$, Val46$_G$, Val61$_G$, Phe66$_G$) in SbzG correspond to Phe41$_K$, Met42$_K$, Phe45$_K$, Val46$_K$, Leu61$_K$ and Phe66$_K$ in SbzK (Supplementary Fig. S23). Furthermore, Glu39, which forms a salt bridge with Arg121 of SbzI, is also conserved in SbzK. These conservations of surface residues should be the reason why SbzI accepts SbzK as a partner protein. Our substrate specificity analysis of SbzI for acyl-donors indicated that the enzyme accepts fatty acyl-CPs and aminoacyl-CPs as substrates, in addition to 2-SA-CP. Acyl-CoA analogs with high polarity, such as malonyl-CP and succinyl-CP, were not accepted by SbzI, probably due to the highly hydrophobic environment of the 2-SA binding site.

GNAT enzymes usually employ an acid/base mechanism for the direct acyl-transfer reactions[2]. A catalytic residue, such as glutamate, aspartate, or histidine, abstracts a proton from the substrate amine, followed by a nucleophilic attack from the activated amino group on the thioester carbonyl carbon to form a tetrahedral intermediate. A general acid, such as a tyrosine or cysteine residue, then protonates the thiolate anion of CoA (Fig. 5A). In contrast, some specific GNAT enzymes adopt an acid/base independent mechanism. For example, FemX$_{Wv}$ from *Weissella viridescens*, which catalyzes L-Ala transfer from Ala-tRNA$_{Ala}$ to the side-chain amine of an L-Lys residue in the peptidoglycan precursor UDP-MurNAc-pentapeptide, does not utilize the residue for proton abstraction or protonation. Instead, stabilization of the tetrahedral intermediate and proton shuttling with the C3'-hydroxyl group of the adenosine moiety facilitate the aminoacyl transfer reaction[57] (Fig. 5B).

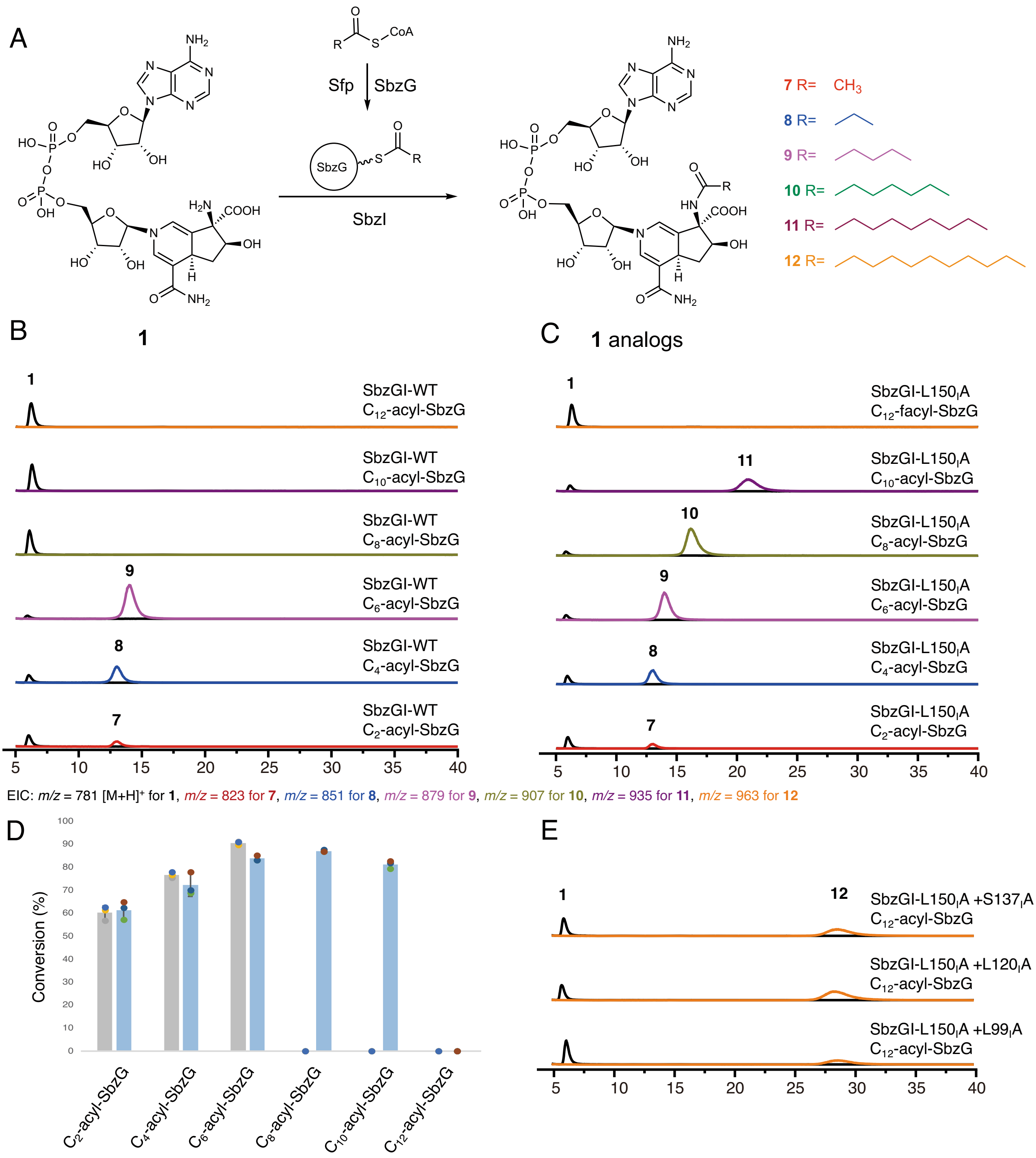

Fig. 4 | Substrate scope of SbzI and engineering the substrate selectivity of SbzI. **A** Enzyme reaction of SbzI with different lengths of fatty acyl-SbzG substrates. **B**, **C** LC-MS profiles of the enzyme reaction products of (**B**) wild type SbzGI and (**C**) SbzGI L150$_I$A variant with different lengths of fatty acyl-SbzG substrates. **D** Comparison of the activities of wild type SbzGI and SbzGI L150$_I$A variant. **E** LC-MS profiles of the enzyme reaction products of SbzGI double variants toward the C$_{12}$-acyl-SbzG substrate. All reactions were performed in triplicates. Data are presented as mean values, and the error bars indicate standard deviations (SD).

Interestingly, although Glu138$_I$ is located where the catalytic glutamate residue is found in other GNAT proteins[2], the E138$_I$A variant exhibited activity comparable to that of wild-type SbzI. The local pKa prediction by MolGpKa[58] suggested that the pKa of the C1 amino group of compound **1** is 7.0. This observation suggests that the C1 amino group is deprotonated under the reaction conditions (pH 8.0), and therefore, no general base is required in the catalytic pocket. Furthermore, residues that could potentially act as a general acid were not identified around the sulfhydryl group of the Ppant arm. Instead, the docking model with compound **1** suggested that the C2 hydroxy group is located close to the sulfhydryl group of the Ppant arm. The predicted pKa of the C2 hydroxyl group is 11.1, similar to that of a Tyr residue (pKa = ~10). Hence, the hydroxyl group in compound **1** may be important for both the stabilization of the tetrahedral intermediate and the proton shuttling to facilitate the acyl transfer reaction. It is also possible that the C2 hydroxy group facilitates the optimal positioning of the thioester group for nucleophilic attack and oxyanion stabilization. These hypotheses are consistent with previous in vitro assays, as compounds **5** and **6**, lacking the C2 hydroxyl group compared to **1**, are not accepted by SbzI.

Based on these observations, we propose the reaction mechanism of SbzI, which is different from classical GNAT enzymes, as follows (Fig. 5C): The acyl acceptor 6-azatetrahydroindane dinucleotide **1** binds in the active site, and the position of the amino acid moiety is determined by a salt bridge network involving Arg48$_I$ and Asp34$_I$. Subsequently, the amino group of **1** undergoes a direct nucleophilic attack on the thioester of the CP-tethered 2-SA, resulting in the formation of a tetrahedral intermediate. Finally, proton shuttling with the C2-hydroxyl group of compound **1** facilitates the acyl transfer reaction and the release of the Ppant arm-SH from the tetrahedral intermediate, to yield the product **2**.

In conclusion, our structural and functional analyses of GNAT SbzI and CP SbzG have provided the structural basis for the recognition of the sulfonamide group of 2-SA in the biosynthesis of altemicidin and insight into how some CP-dependent GNAT enzymes recognize an acyl-CP instead of an acyl-CoA substrate. Furthermore, structure-based enzyme engineering rationally expanded the substrate scope for the acyl donor of SbzI. The acyl substrate for incorporation in altemicidin biosynthesis is determined by the adenylation enzyme SbzL, which strictly recognizes 2-SA[45]. Further development of engineered SbzL and SbzI proteins with altered substrate scopes will generate unnatural, novel azaindane dinucleotide derivatives for future drug discovery.

Methods

General remarks

Oligonucleotide primers were purchased from Eurofins Genomics. Other chemicals were purchased from Wako Chemical, Ltd. (Tokyo, Japan). Analytical grade solvents were purchased from Kanto Chemical Co., Inc. (Tokyo, Japan). The LCMS data were obtained by using a Liquid Chromatograph Mass Spectrometer LCMS-8045 attached to a High Performance Liquid Chromatograph LC-2050C LT system (Shimadzu).

Plasmid construction and mutagenesis

The DNA sequences encoding SbzG and SbzI were cloned from the genomic DNA (gDNA) of *Streptomyces sioyaensis* SA-1758 and inserted into the pET28a(+) vector with an N-terminal 6xHis tag. A protein linker (GGGGS) was introduced using primers according to the protocol from the In-Fusion® HD Cloning Kit (Takara). For the in vivo modification of SbzGI, the pACYCDuet-SbzGI-sfp plasmid was constructed to coexpress SbzGI and sfp in *E. coli*. The DNA encoding sfp from *Bacillus subtilis* was cloned into the pACYCDuet vector. Site-directed mutagenesis was performed using a PCR-based method. Initially, PCR was carried out with two primers containing the desired mutation(s) and a 15-base overlap, using a KOD FX DNA Polymerase kit (TOYOBO). After PCR, the products were confirmed by DNA gel electrophoresis, and the correct bands were extracted with a Wizard® SV Gel and PCR Clean-Up System (Promega). The extracted products were then transformed into competent *E. coli* DH5α cells. The mutations were confirmed by DNA sequencing (Eurofins).

Protein expression and purification

The protein expression plasmids were transformed into competent *E. coli* BL21(DE3) cells. After overnight incubation at 37 °C in a shaker, the seed cultures were used to inoculate 1 L of Lysogeny broth (LB) medium containing antibiotics (50 µg/mL kanamycin for pET28a (+) plasmids, 50 µg/mL chloramphenicol for pACYCDuet plasmids) and cultured at 37 °C with shaking at 160 rpm. When the OD_{600} reached 0.5–0.7, the LB medium was cooled on ice for 15 min, and then IPTG was added to a final concentration of 500 µM. The cultures were further incubated for 18 h at 18 °C with shaking at 160 rpm. Cells were harvested by centrifugation and stored at − 30 °C. The cells were resuspended in buffer A (50 mM Tris-HCl, pH 8, 300 mM NaCl, 10 mM imidazole, and 10% glycerol) and then lysed by sonication. The supernatant was obtained by centrifugation and loaded onto a Ni-NTA gravity column pre-equilibrated with buffer B (50 mM Tris-HCl, pH 8, 300 mM NaCl, 20 mM imidazole, and 10% glycerol). The supernatant was incubated on the Ni-NTA gravity column for 15 min and then flowed through the column. After washing with 50 column volumes of buffer B, His-tagged proteins were eluted with buffer C (50 mM Tris-HCl, pH 8, 300 mM NaCl, 500 mM imidazole, and 10% glycerol). Buffer exchange of the eluted protein into the final stock buffer D (25 mM Tris-HCl, pH 8, 50 mM NaCl, 2 mM dithiothreitol) was performed with a PD-10 Desalting Column (Cytiva). Fractions of interest were concentrated using Amicon® Ultra Centrifugal Filters, and the protein concentration was measured by UV absorption at 280 nm. For crystallization screening, the protein was further purified by size-exclusion chromatography. The protein was loaded onto an ÄKTA™ FPLC (Cytiva) with a Superdex™ 200 Increase 10/300 GL gel filtration column pre-equilibrated with buffer D. A single peak was collected in a 96-well deep well plate, and the purity was analyzed by sodium dodecylsulfate polyacrylamide gel electrophoresis (SDS-PAGE). After concentration, the protein was stored at − 80 °C.

Pull-down assay

His-tagged SbzI and SbzG (without tag) were introduced into the pACYCDuet vector and co-expressed in *E. coli* BLR (DE3). After loading to Ni-NTA gravity column, the column was washed with wash buffer (50 mM Tris-HCl, pH 8, 300 mM NaCl, 20 mM imidazole, and 10% glycerol) for 50 column volume, then eluted by elution buffer (50 mM Tris-HCl, pH 8, 300 mM NaCl, 500 mM imidazole, and 10% glycerol) for 5 column volume. Proteins in each fraction were analyzed by SDS-PAGE.

Cross-linking assay

SbzI SSSC variants and the holo-SbzG C80$_G$S variants were expressed as a general protocol. After being purified by Ni-NTA gravity column, the buffer was exchanged to the cross-linking buffer (50 mM Tris-HCl, pH 7.3, 300 mM NaCl, 5 mM EDTA, 10% glycerol) with a PD-10 Desalting Column (Cytiva). Cross-linking assay was performed as follows: SbzI variants 5 µM, SbzG variants 10 µM, and BMOE 100 µM were mixed and incubated for 0, 5, and 30 min at room temperature. Reactions were quenched by SDS-PAGE loading buffer and then analyzed by SDS-PAGE.

ITC analysis

His-tagged SbzI (WT) and His-tagged SbzG (WT and variants) were purified as described above. After Ni-NTA purification, the buffer was exchanged for the ITC buffer (50 mM Tris-HCl, pH 8, 300 mM NaCl, 10% glycerol) with a PD-10 Desalting Column (Cytiva). ITC assays were performed by using MicroCal iTC200(Malvern). SbzI 0.15 mM and SbzG 1.5 mM were used for analysis. ITC cell temperature was set to 27 °C, reference power was set to 8 µcal/s. Data analysis was done by Origin.

X-ray Crystallography

Initial crystallization screening was performed using the Wizard Classic I and II kits (Molecular Dimensions), the PEG/Ion Screen kit (Hampton Research), the Crystal Screen kit (Hampton Research), and the MCC kit. Crystallization drops were prepared at 20 °C according to the sitting drop vapor diffusion protocol, by mixing 0.5 µL of protein solution with 0.5 µL of reservoir solution in the crystal wells of an Intelli-Plate 96-2 Low Profile (Hampton Research). For the screening, 12.8 mg/mL of holo-SbzGI and 15 mg/mL of SbzI were used. Crystals appeared within 3–7 days. After obtaining the initial crystals, the conditions were further optimized using the Additive Screen kit (Hampton Research). Optimization involved adjusting the concentrations of protein, salt, and

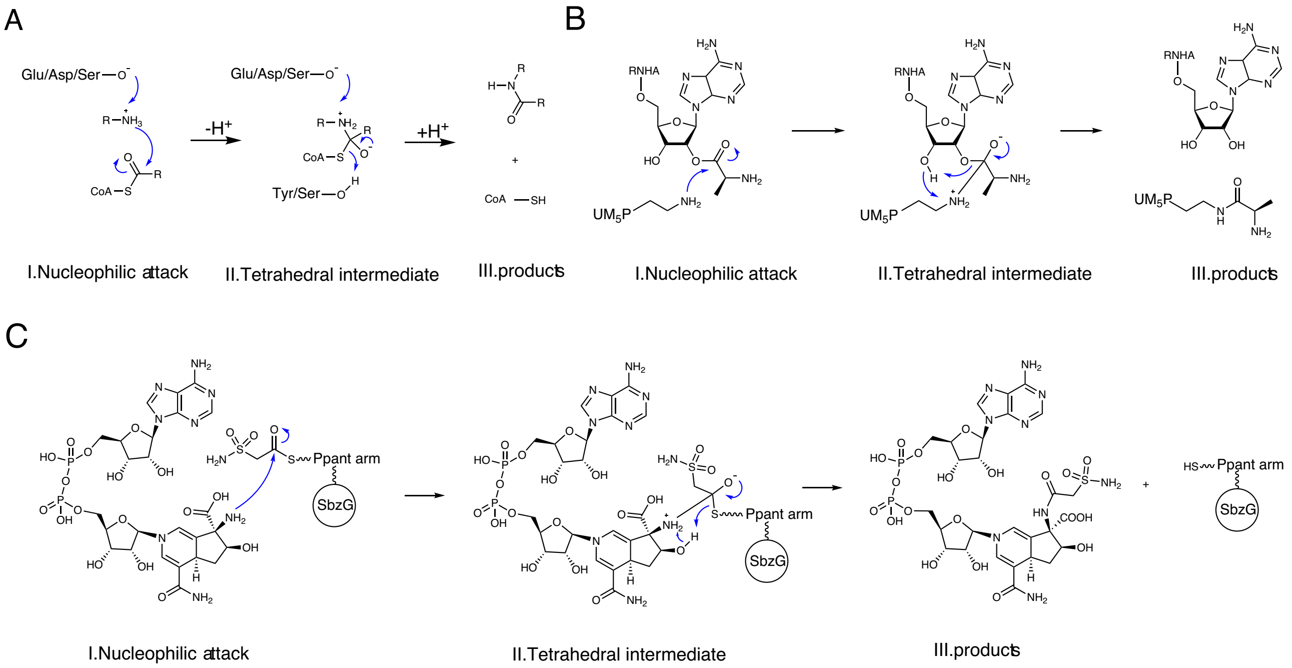

Fig. 5 | Proposed mechanisms for GNATs. **A** Acid/base mechanism for general GNAT proteins. **B** Acid/base independent mechanism for FemX$_{Wv}$ from *Weissella viridescens*. **C** Proposed mechanism for SbzI.

precipitating reagent. The best-resolution crystals were obtained under the following conditions: For SbzI: 0.1 M Tris-HCl, pH 8.0, 0.2 M KSCN, 25% (w/v) PEG 3350. For SbzGI: 0.1 M MES, pH 6.5, 0.2 M KSCN, 15% (w/v) PEG 8000, 3% (v/v) ethylene glycol. The crystals were transferred into a cryoprotectant solution (reservoir solution with 25% (v/v) glycerol) and then flash-cooled at − 173 °C in liquid nitrogen. The X-ray diffraction data sets were collected at BL-1A (Photon Factory, Tsukuba, Japan), using a beam wavelength of 1.1 Å, and BL45XU (SPring-8, Harima, Hyogo, Japan), using a beam wavelength of 1.0 Å. The diffraction data sets were processed and scaled using the XDS program package[59] and Aimless[60] in CCP4. The initial phases of the SbzI structures were determined by molecular replacement, using the model structures of SbzI constructed by ColabFold[61] as the search models. Molecular replacement was performed with Phaser in PHENIX[62]. The initial phases were further improved with AutoBuild in PHENIX[63]. The structures were modified manually with Coot[64] and refined with PHENIX.refine[65]. The final crystal data and intensity statistics are summarized in Supplementary Table 1. A structural similarity search was performed, using the Dali program[66] server. All crystallographic figures were prepared with PyMOL (DeLano Scientific, http://www.pymol.org). The high B-factor of the SbzGI structure is possibly due to the flexibility of the loop between SbzI and SbzG. Despite the fusion of SbzG and SbzI, the interaction may still be weak, and the conformation of SbzGI is not completely fixed in the crystal. Indeed, SbzG of monomer B is not involved in the crystal packing interactions. Furthermore, due to poor density in monomer B, water molecules could not be added to the monomer B region or to the interface between monomers A and B.

Preparation of docking model

The three-dimensional model structures of compound **1** were generated by the CHEM3D ULTRA 10 program (Cambridge Soft), and their geometries were optimized with the elbow tool in Phenix. The docking model was constructed by using HADDOCK ver 2.3[67,68]. First, Ppant-tethered 2-SA was docked into the active site of the SbzGI complex, and the conformation of the Ppant moiety was manually modified to resemble that of the Ppant arm in the crystal structure. The conformation of Ppant-tethered 2-SA was further refined using COOT to avoid close contact between the 2-SA moiety and the active site residues. Subsequently, compound **1** was docked into the active site using the 2-SA docking model as the input protein. For docking compound **1**, the active site residues Arg48$_I$, Glu138$_I$, Asn140$_I$, and Arg170$_I$ were set as active residues, and the docking was performed with default settings. The docking model was then validated through MD simulation as described below.

MD simulation

The docking model of the SbzG-SbzI fusion protein in complex with compound **1** and Ppant-tethered 2-SA, described in the "*Preparation of docking model*" section, was used as the initial structure. SbzG and SbzI were treated as individual subunits by removing the linker connecting the two proteins. Amino acid residues ranging from 1 to 84 of SbzG and 1 to 178 of SbzI were employed for the MD simulations. The undetermined loop structure of SbzG (residues from 21 to 23) was modeled using Modeler 10.4[69]. C-termini of SbzG and SbzI were capped with *N*-methyl amide (NME) groups due to missing regions. The protonation states of the titratable residues were estimated using the H + + server[70] at pH 8.0 and salinity of 0.1 M.

The geometry of compound **1** was optimized at B3LYP/6-31 G + (d,p) level using Gaussian 16 rev. C.02[71], followed by a single-point calculation at HF/6-31 G(d) level to calculate the electrostatic potential around the molecule. The atomic charges that fit the electrostatic potential were calculated using the Antechamber[72] module with the Restrained Electrostatic Potential (RESP) method[73]. The protonation state of the C1 amino group was set as an unprotonated form ($R{-}NH_2$), based on the p*K*a estimation described in the main text. To generate the parameter and topology files for the serine residue modified by Ppant-tethered 2-SA, the modified residue was decomposed into two fragments, phosphoserine and the 2-SA-attached pantetheine moiety excluding the terminal hydroxy group. The boundaries between the two fragments were capped with hydrogen atoms. The parameters and topology files for singly protonated phosphoserine (S1P) were obtained from the Amber Parameter Database[74]. The latter fragment was parameterized through geometry optimization and subsequent RESP calculation, following the same procedure as compound **1**. The parameter and topology files for the whole structure of the modified residue were generated by combining those of the two fragments.

The resulting complex was immersed in a box of OPC water molecules[75] with a buffer width of more than 10 Å, containing approximately 0.1 M Na^+ and Cl^- ions. Solvation was performed using the AMBER LEaP module. The initial system was a cubic box of 83 Å × 83 Å × 83 Å, consisting of 15,913 water molecules, 33 Na^+ ions, 25 Cl^- ions, and a 265-residue SbzGI complex including a compound **1** molecule, a serine residue modified with Ppant-tethered 2-SA, two *C*-terminal NME capping molecules. The number of Na^+ and Cl^- ions was determined based on the SPLIT method[76]. The AMBER ff19SB[77] and GAFF2 force fields were applied to the protein and the substrates, respectively. Subsequent MD simulations were performed using AMBER24[78,79] as follows.

Energy minimization was carried out for 5500 steps, during which position restraints were imposed on the non-hydrogen atoms of the protein, and the force constant was gradually decreased from 10 kcal mol^{-1} $Å^{-2}$ to 5, 2, 1, 0.5, 0.2, and 0 kcal mol^{-1} $Å^{-2}$. The system was then heated from 10 K to 298.15 K over a 500 ps *NVT* simulation using the Langevin thermostat with a collision frequency of 2.0 ps^{-1} and with position restraints of 10 kcal mol^{-1} $Å^{-2}$ on the non-hydrogen atoms of the protein. The *NVT* simulation was continued for another 500 ps. The equilibration and subsequent production run were conducted in an *NPT* ensemble, employing the Bussi thermostat[80] and the Monte Carlo barostat[81] to maintain the temperature and pressure at 298.15 K and 1.013 bar, respectively. The equilibration was performed for 25 ns with harmonic position restraints on the non-hydrogen atoms of the protein, and the force constant was gradually decreased from 10 kcal mol^{-1} $Å^{-2}$ to 0 kcal/mol^{-1} $Å^{-2}$ in a similar way to the energy minimization step. The equilibration was continued for 100 ns without restraints to further relax the system. The production run was then conducted for 1 µs. Long-range electrostatic interactions were treated using the particle mesh Ewald method[82]. A non-bonded cutoff distance was set to 8 Å and 10 Å during the equilibration and the production run, respectively, for both van der Waals and direct space electrostatic interactions. A 2-fs time step was used for the simulations, where the SHAKE algorithm[83] was applied to constrain the bonds involving hydrogen atoms. MD simulations, consisting of energy minimization, equilibration, and production run, were independently performed three times. The resulting trajectories were processed and analyzed every 200 ps using CPPTRAJ[84]. Root mean square deviation (RMSD) was calculated against the initial energy-minimized structure.

Preparation of compound 1[46]

Compound **1** was prepared by a PsePQ reaction conducted as follows: a 60 × 250 µL scale reaction mixture containing 1 mM SAM, 1 mM NAD^+, 0.2 mM PLP, and 18.6 µM PsePQ in 50 mM KP buffer (pH 7.8), was incubated at 30 °C for 2 h. Subsequently, 2.5 mM α-ketoglutaric acid, 2.0 mM L-ascorbic acid, 0.1 mM $FeSO_4$, and 20 µM PseQ were added, and the mixture was incubated at 30 °C for another 2 h. The reaction mixture was freeze-dried and subjected to column chromatography (Sephadex LH-20, eluent: water) at 4 °C. Fractions containing compound 1 were collected and further purified by semi-preparative HPLC using a HILIC Cosmosil column (10.0 mm I.D. × 250 mm), with a solvent gradient of 50 mM ammonium formate (pH 9.0): acetonitrile from 100:0 to 0:100. Fractions containing compound **1** were collected and lyophilized to yield pure compound **1** as a white powder (2 mg).

Preparation of compound 3

Compound **3** was enzymatically synthesized from compound **1**. The phosphate bond cleavage reaction was performed on a 100 × 60 µl scale, in a mixture containing 17 mM EDTA, 83 mM $MgCl_2$, 0.5 mM compound 1, 0.006 units/µl phosphodiesterase I (Millipore Sigma), 70 units/µl Bacterial Alkaline Phosphatase (BAP, Thermo Fisher), and 6 µl of 10 × BAP buffer in 500 mM Tris-HCl (pH 7.5) at 30 °C for 1 h. The reaction was quenched by adding 60 µl of 100% acetonitrile, followed by the removal of precipitated proteins. Compound **3** was purified by HPLC under the same conditions as those used for compound **1**, yielding 1.0 mg of a white powder after solvent removal in vacuo.

Preparation of compound 4

A reaction mixture (500 µl) containing 50 mM altemicidin in assay buffer (4 M HCl) was incubated at 50 °C overnight. After lyophilization, the mixture was redissolved in distilled water and purified using the same HPLC method as described above, yielding 1.6 mg of pure white powder (17.7%).

Preparation of compounds 5 and 6

The reaction was carried out on a 60 × 250 µl scale, in a mixture containing 1 mM SAM, 1 mM NAD^+, 0.2 mM PLP, and 18.6 µM PsePQ[46] in 50 mM KP buffer (pH 7.8) at 30 °C for 2 h. The reaction was quenched with 250 µl of 100% acetonitrile, freeze-dried, and subjected to column chromatography (Sephadex LH-20, eluent: water) at 4 °C. Fractions containing compound **5** were combined and further purified by semi-preparative HPLC. After lyophilization, 2.3 mg of compound **5** was obtained. The phosphate bond cleavage reaction was then conducted as described above, using compound **5** as the substrate, resulting in 1.0 mg of compound **6**.

In vitro assay of SbzGI and variants

Firstly, apo-SbzGI was modified in vitro with CoA to obtain holo-SbzGI, using the Sfp protein in the following reaction mixture: 50 mM HEPES (pH 8), 40 µM apo-SbzGI (WT or variants), 15 µM Sfp, 1 mM coenzyme A, 1 mM dithiothreitol, and 10 mM $MgCl_2$, which was incubated at 24 °C for 1 h. Then, the activity of holo-SbzGI (WT or variants) was evaluated in vitro in the following reaction mixture: 50 mM HEPES (pH 8), 20 µM holo-SbzGI (WT or variants), 20 µM SbzL, 1.5 mM compound **1**, 1 mM 2-sulfamoylacetyl acid, 1 mM ATP, and 1 mM $MgCl_2$, which was incubated at 24 °C for 30 min. The reaction was quenched by adding an equivalent volume of methanol and then centrifuged at 20,000 × *g* for 30 min to remove all precipitates. The reaction was analyzed using a Liquid Chromatograph Mass Spectrometer (LCMS-8045) attached to a High-Performance Liquid Chromatograph (LC-2050C LT system, Shimadzu) with a HILICpak VG-50 2D column (Shodex). An isocratic method of 30% CH_3CN–50 mM ammonium formate (pH 9) over 30 or 60 min was used, at a flow rate of 0.2 mL/min. Substrates and products were analyzed under EIC in the positive mode. The data were analyzed by LabSolutions (Shimadzu). For acyl-CoA substrates, the reaction was performed in 50 mM HEPES, pH 8, 200 µM apo SbzGI (WT or variants), 15 µM Sfp, 0.5 mM acyl-CoA substrate, 1.5 mM compound **1**, 1 mM dithiothreitol, and 10 mM $MgCl_2$, and incubated at 24 °C for 1 h. For acid substrates, the reaction was performed in 50 mM HEPES, pH 8, 200 µM holo-SbzGI (WT or variants), 20 µM SbzL, 1.5 mM compound **1**, 1 mM acid substrates, 1 mM ATP, and 1 mM $MgCl_2$, and incubated at 24 °C overnight. The reaction was quenched by the addition of an equivalent volume of methanol and then centrifuged at 20,000 × *g* for 30 min to remove all precipitates. The reaction was analyzed by a Liquid Chromatograph Mass Spectrometer (LCMS-8045) attached to a High Performance Liquid Chromatograph (LC-2050C LT system, Shimadzu), with a HILICpak VG-50 2D column (Shodex), using isocratic elution with 30% CH_3CN–50 mM ammonium formate pH = 9 over 30 min or 60 min, at a flow rate of 0.2 mL/min. Substrates and products were analyzed under EIC in the positive mode. All reactions were repeated more than three times with similar results.

Reporting summary

Further information on research design is available in the Nature Portfolio Reporting Summary linked to this article.

Data availability

The data generated in this study are provided in the article, Supplementary Information, and Source Data file. The crystallographic data that support the findings of this study are available in the Protein Data Bank (http://www.rcsb.org) under accession codes 8ZT3 (for SbzI) [https://doi.org/10.2210/pdb8zt3/pdb] and 8ZT4 (for SbzGI) [https://doi.org/10.2210/pdb8zt4/pdb]. The MD simulation data of complex models of SbzGI and compound **1** are freely available at Zenodo (https://zenodo.org/records/14233270). Source data are provided in this paper.

References

1. Neuwald, A. F. & Landsman, D. GCN5-related histone N-acetyltransferases belong to a diverse superfamily that includes the yeast SPT10 protein. *Trends Biochem. Sci.* **22**, 154–155 (1997).
2. Salah Ud-Din, A. I., Tikhomirova, A. & Roujeinikova, A. Structure and functional diversity of GCN5-related N-acetyltransferases (GNAT). *Int. J. Mol. Sci.* **17**, 1018 (2016).
3. VanDrisse, C. M. & Escalante-Semerena, J. C. Small-molecule acetylation controls the degradation of benzoate and photosynthesis in Rhodopseudomonas palustris. *mBio* **9**, e01895–18 (2018).
4. Trievel, R. C. et al. Crystal structure and mechanism of histone acetylation of the yeast GCN5 transcriptional coactivator. *Proc. Natl. Acad. Sci. USA* **96**, 8931–8936 (1999).
5. Rojas, J. R. et al. Structure of *Tetrahymena* GCN5 bound to coenzyme A and a histone H3 peptide. *Nature* **401**, 93–98 (1999).
6. Lin, Y. X., Fletcher, C. M., Zhou, J. X., Allis, C. D. & Wagner, G. Solution structure of the catalytic domain of GCN5 histone acetyltransferase bound to coenzyme A. *Nature* **400**, 86–89 (1999).
7. Yu, Y. et al. Novel D-glutamate catabolic pathway in marine Proteobacteria and halophilic archaea. *ISME J.* **17**, 537–548 (2023).
8. Toplak, M., Nagel, A., Frensch, B., Lechtenberg, T. & Teufel, R. An acetyltransferase controls the metabolic flux in rubromycin polyketide biosynthesis by direct modulation of redox tailoring enzymes. *Chem. Sci.* **13**, 7157–7164 (2022).
9. Jeter, V. L. & Escalante-Semerena, J. C. Sirtuin-dependent reversible Lysine acetylation controls the activity of acetyl coenzyme a synthetase in campylobacter jejuni. *J. Bacteriol.* **203**, e0033321 (2021).
10. Parks, A. R. & Escalante-Semerena, J. C. Modulation of the bacterial CobB sirtuin deacylase activity by N-terminal acetylation. *Proc. Natl. Acad. Sci. USA* **117**, 15895–15901 (2020).
11. Radhakrishnan, L., Dani, R., Navabshan, I., Jamal, S. & Ahmed, N. Targeting aminoglycoside acetyltransferase activity of mycobacterium tuberculosis (H37Rv) derived Eis (Enhanced Intracellular Survival) protein with quercetin. *Protein J.* **43**, 12–23 (2023).
12. Dang, T. et al. Molecular basis of antibiotic self-resistance in a bee larvae pathogen. *Nat. Commun.* **13**, 2349 (2022).
13. Verma, A., Nayek, A., Kumar, A., Singh, R. & Salotra, P. Elucidation of role of an acetyltransferase like protein in paromomycin resistance in Leishmania donovani using in silico and in vitro approaches. *J. Biomol. Struct. Dyn.* **38**, 4449–4460 (2020).
14. Burckhardt, R. M. & Escalante-Semerena, J. C. Insights into the function of the N-acetyltransferase SatA that detoxifies streptothricin in bacillus subtilis and bacillus anthracis. *Appl. Environ. Microbiol.* **85**, e03029–18 (2019).
15. Xu, Z. et al. Structural and functional survey of environmental aminoglycoside acetyltransferases reveals functionality of resistance enzymes. *ACS Infect. Dis.* **3**, 653–665 (2017).
16. Stogios, P. J. et al. Structural and biochemical characterization of acinetobacter spp. aminoglycoside acetyltransferases highlights functional and evolutionary variation among antibiotic resistance enzymes. *ACS Infect. Dis.* **3**, 132–143 (2017).
17. Wolf, E. et al. Crystal structure of a GCN5-related N-acetyltransferase. *Cell* **94**, 439–449 (1998).
18. Ma, X., Jiang, K., Zhou, C., Xue, Y. & Ma, Y. Identification and characterization of a novel GNAT superfamily N(alpha)-acetyltransferase from Salinicoccus halodurans H3B36. *Microb. Biotechnol.* **15**, 1652–1665 (2022).
19. Alsarraf, H. et al. Biochemical, structural, and functional studies reveal that MAB_4324c from *Mycobacterium abscessus* is an active tandem repeat N-acetyltransferase. *FEBS Lett.* **596**, 1516–1532 (2022).
20. Xu, H., Hegde, S. S. & Blanchard, J. S. Reversible acetylation and inactivation of *Mycobacterium tuberculosis* acetyl-CoA synthetase is dependent on cAMP. *Biochemistry* **50**, 5883–5892 (2011).
21. Lihua, Y. et al. N-acetyltransferase gene NATA1 from *Vigna angularis* confers resistance against Uromyces vignae infection. *Physiol. Mol. Plant Pathol.* **113**, 101585 (2021).
22. Filippova, E. V. et al. Crystal structure of the novel PaiA N-acetyltransferase from *Thermoplasma acidophilum* involved in the negative control of sporulation and degradative enzyme production. *Proteins* **79**, 2566–2577 (2011).
23. Tsimbalyuk, S., Shornikov, A., Thi Bich Le, V., Kuhn, M. L. & Forwood, J. K. SpeG polyamine acetyltransferase enzyme from Bacillus thuringiensis forms a dodecameric structure and exhibits high catalytic efficiency. *J. Struct. Biol.* **210**, 107506 (2020).
24. Murakami, T. et al. The bialaphos biosynthetic genes of *Streptomyces hygroscopicus:* Molecular cloning and characterization of the gene cluster. *Mol. Gen. Genet.* **205**, 42–50 (1986).
25. Thompson, C. J. et al. Characterization of the herbicide-resistance gene bar from *Streptomyces hygroscopicus*. *Embo J.* **6**, 2519–2523 (1987).
26. Wohlleben, W. et al. Nucleotide sequence of the phosphinothricin N-acetyltransferase gene from Streptomyces viridochromogenes Tü494 and its expression in Nicotiana tabacum. *Gene* **70**, 25–37 (1988).
27. Vetting, M. W., Roderick, S. L., Yu, M. & Blanchard, J. S. Crystal structure of mycothiol synthase (Rv0819) from *Mycobacterium tuberculosis* shows structural homology to the GNAT, family of N-acetyltransferases. *Protein Sci.* **12**, 1954–1959 (2003).
28. Vetting, M. W., Yu, M., Rendle, P. M. & Blanchard, J. S. The substrate-induced conformational change of *Mycobacterium tuberculosis* mycothiol synthase. *J. Biol. Chem.* **281**, 2795–2802 (2006).
29. Piel, J., Wen, G., Platzer, M. & Hui, D. Unprecedented diversity of catalytic domains in the first four modules of the putative pederin polyketide synthase. *Chembiochem* **5**, 93–98 (2004).
30. Young, J. et al. Elucidation of gephyronic acid biosynthetic pathway revealed unexpected SAM-dependent methylations. *J. Nat. Prod.* **76**, 2269–2276 (2013).
31. Moebius, N. et al. Biosynthesis of the respiratory toxin bongkrekic scid in the pathogenic bacterium *Burkholderia gladioli*. *Chem. Biol.* **19**, 1164–1174 (2012).
32. Simunovic, V. et al. Myxovirescin A biosynthesis is directed by hybrid polyketide synthases/nonribosomal peptide synthetase, 3-hydroxy-3-methylglutaryl-CoA synthases, and trans-acting acyltransferases. *Chembiochem* **7**, 1206–1220 (2006).
33. Piel, J. et al. Antitumor polyketide biosynthesis by an uncultivated bacterial symbiont of the marine sponge *Theonella swinhoei*. *Proc. Natl. Acad. Sci. USA* **101**, 16222–16227 (2004).
34. Piel, J. A polyketide synthase-peptide synthetase gene cluster from an uncultured bacterial symbiont of *Paederus* beetles. *Proc. Natl. Acad. Sci. USA* **99**, 14002–14007 (2002).
35. Mattheus, W. et al. Isolation and purification of a new kalimantacin/batumin-related polyketide antibiotic and elucidation of its biosynthesis gene cluster. *Chem. Biol.* **17**, 149–159 (2010).
36. Chang, Z. X. et al. Biosynthetic pathway and gene cluster analysis of curacin A, an antitubulin natural product from the tropical marine cyanobacterium *Lyngbya majuscula*. *J. Nat. Prod.* **67**, 1356–1367 (2004).

37. Grindberg, R. V. et al. Single cell genome amplification accelerates identification of the apratoxin biosynthetic pathway from a complex microbial assemblage. *Plos ONE* **6**, e18565 (2011).
38. Hubrich, F. et al. Ribosomally derived lipopeptides containing distinct fatty acyl moieties. *Proc. Natl. Acad. Sci. USA* **119**, e2113120119 (2022).
39. Kozakai, R. et al. Acyltransferase that catalyses the condensation of polyketide and peptide moieties of goadvionin hybrid lipopeptides. *Nat. Chem.* **12**, 869–877 (2020).
40. Skiba, M. A. et al. Repurposing the GNAT Fold in the Initiation of Polyketide Biosynthesis. *Structure* **28**, 63–74 (2020).
41. Gu, L. C. et al. GNAT-like strategy for polyketide chain initiation. *Science* **318**, 970–974 (2007).
42. Chun, S. W., Hinze, M. E., Skiba, M. A. & Narayan, A. R. H. Chemistry of a unique polyketide-like synthase. *J. Am. Chem. Soc.* **140**, 2430–2433 (2018).
43. Van Wagoner, R. M. & Clardy, J. FeeM, an N-acyl amino acid synthase from an uncultured soil microbe: structure, mechanism, and acyl carrier protein binding. *Structure* **14**, 1425–1435 (2006).
44. Takahashi, A., Kurasawa, S., Ikeda, D., Okami, Y. & Takeuchi, T. Altemicidin, a new acaricidal and antitumor substance. I. Taxonomy, fermentation, isolation and physico-chemical and biological properties. *J. Antibiot.* **42**, 1556–1561 (1989).
45. Hu, Z., Awakawa, T., Ma, Z. & Abe, I. Aminoacyl sulfonamide assembly in SB-203208 biosynthesis. *Nat. Commun.* **10**, 184 (2019).
46. Barra, L. et al. b-NAD as a building block in natural product biosynthesis. *Nature* **600**, 754–758 (2021).
47. Ma, C. et al. Structure of *Thermoplasma volcanium* Ard1 belongs to N-acetyltransferase family member suggesting multiple ligand binding modes with acetyl coenzyme A and coenzyme A. *Biochim. Biophys. Acta* **1844**, 1790–1797 (2014).
48. Vetting, M. W., Bareich, D. C., Yu, M. & Blanchard, J. S. Crystal structure of RimI from *Salmonella typhimurium* LT2, the GNAT responsible for N(alpha)-acetylation of ribosomal protein S18. *Protein Sci.* **17**, 1781–1790 (2008).
49. Burckhardt, R. M. & Escalante-Semerena, J. C. Small-molecule acetylation by GCN5-related N-acetyltransferases in bacteria. *Microbiol. Mol. Biol. Rev.* **84**, e00090–19 (2020).
50. Chen, X., Zaro, J. L. & Shen, W. C. Fusion protein linkers: property, design and functionality. *Adv. Drug. Deliv. Rev.* **65**, 1357–1369 (2013).
51. Mocibob, M., Ivic, N., Luic, M. & Weygand-Durasevic, I. Adaptation of sminoacyl-tRNA dynthetase catalytic core to carrier protein aminoacylation. *Structure* **21**, 614–626 (2013).
52. Miyanaga, A., Iwasawa, S., Shinohara, Y., Kudo, F. & Eguchi, T. Structure-based analysis of the molecular interactions between acyltransferase and acyl carrier protein in vicenistatin biosynthesis. *Proc. Natl. Acad. Sci. USA* **113**, 1802–1807 (2016).
53. Zhang, L. et al. Malonyl-CoA: acyl carrier protein transacylase from Helicobacter pylori: Crystal structure and its interaction with acyl carrier protein. *Protein Sci.* **16**, 1184–1192 (2007).
54. Quadri, L. E. N. et al. Characterization of Sfp, a *Bacillus subtilis* phosphopantetheinyl transferase for peptidyl carrier protein domains in peptide synthetases. *Biochemistry* **37**, 1585–1595 (1998).
55. Byers, D. M. & Gong, H. S. Acyl carrier protein: structure-function relationships in a conserved multifunctional protein family. *Biochem. Cell Biol.* **85**, 649–662 (2007).
56. Mori, T. et al. Molecular basis for carrier protein-dependent amide bond formation in the biosynthesis of lincosamide antibiotics. *Nat. Catal.* **6**, 531–542 (2023).
57. Fonvielle, M. et al. The structure of FemX(Wv) in complex with a peptidyl-RNA conjugate: mechanism of aminoacyl transfer from Ala-tRNA(Ala) to peptidoglycan precursors. *Angew. Chem. Int. Ed.* **52**, 7278–7281 (2013).
58. Pan, X., Wang, H., Li, C., Zhang, J. Z. H. & Ji, C. MolGpka: A web server for small molecule pK(a) prediction using a graph-convolutional neural network. *J. Chem. Inf. Model.* **61**, 3159–3165 (2021).
59. Kabsch, W. XDS. *Acta Crystallogr. D Biol. Crystallogr.* **66**, 125–132 (2010).
60. Evans, P. R. & Murshudov, G. N. How good are my data and what is the resolution? *Acta Crystallogr. D Biol. Crystallogr.* **69**, 1204–1214 (2013).
61. Mirdita, M. et al. ColabFold: making protein folding accessible to all. *Nat. Methods* **19**, 679–682 (2022).
62. McCoy, A. J. et al. Phaser crystallographic software. *J. Appl. Crystallogr.* **40**, 658–674 (2007).
63. Adams, P. D. et al. PHENIX: a comprehensive Python-based system for macromolecular structure solution. *Acta Crystallogr. D Biol. Crystallogr.* **66**, 213–221 (2010).
64. Emsley, P. & Cowtan, K. Coot: model-building tools for molecular graphics. *Acta Crystallogr. D Biol. Crystallogr.* **60**, 2126–2132 (2004).
65. Afonine, P. V. et al. Towards automated crystallographic structure refinement with phenix.refine. *Acta Crystallogr. D Biol. Crystallogr.* **68**, 352–367 (2012).
66. Holm, L. & Rosenström, P. Dali server: conservation mapping in 3D. *Nucleic. Acids Res.* **38**, W545–W549 (2010).
67. van Zundert, G. C. P. et al. The HADDOCK2.2 Web Server: User-friendly integrative modeling of biomolecular complexes. *J. Mol. Biol.* **428**, 720–725 (2016).
68. Honorato, R. V. et al. Structural biology in the Clouds: The WeNMR-EOSC ecosystem. *Front. Mol. Biosci.* **8**, 729513 (2021).
69. Šali, A. & Blundell, T. L. Comparative protein modelling by satisfaction of spatial restraints. *J. Mol. Biol.* **234**, 779–815 (1993).
70. Gordon, J. C. et al. H++: a server for estimating p*K*as and adding missing hydrogens to macromolecules. *Nucleic Acids Res.* **33**, W368–W371 (2005).
71. Frisch, M. J. et al. Gaussian 16 Revision C.02. *Gaussian, Inc*. (2016).
72. Wang, J., Wang, W., Kollman, P. A. & Case, D. A. Automatic atom type and bond type perception in molecular mechanical calculations. *J. Mol. Graph. Model.* **25**, 247–260 (2006).
73. Bayly, C. I., Cieplak, P., Cornell, W. & Kollman, P. A. A well-behaved electrostatic potential based method using charge restraints for deriving atomic charges: the RESP model. *J. Phys. Chem.* **97**, 10269–10280 (1993).
74. Homeyer, N., Horn, A. H. C., Lanig, H. & Sticht, H. AMBER force-field parameters for phosphorylated amino acids in different protonation states: phosphoserine, phosphothreonine, phosphotyrosine, and phosphohistidine. *J. Mol. Model.* **12**, 281–289 (2006).
75. Izadi, S., Anandakrishnan, R. & Onufriev, A. V. Building water models: A different approach. *J. Phys. Chem. Lett.* **5**, 3863–3871 (2014).
76. Machado, M. R. & Pantano, S. Split the charge difference in two! a rule of thumb for adding proper amounts of ions in MD simulations. *J. Chem. Theory Comput.* **16**, 1367–1372 (2020).
77. Tian, C. et al. ff19SB: Amino-acid-specific protein backbone parameters trained against quantum mechanics energy surfaces in solution. *J. Chem. Theory Comput.* **16**, 528–552 (2020).
78. Case, D. A. et al. *Amber 2024*. (University of California, San Francisco, 2024).
79. Case, D. A. et al. AmberTools. *J. Chem. Inform. Model.* **63**, 6183–6191 (2023).
80. Bussi, G., Donadio, D. & Parrinello, M. Canonical sampling through velocity rescaling. *J. Chem. Phys.* **126**, 014101–014101 (2007).
81. Åqvist, J., Wennerström, P., Nervall, M., Bjelic, S. & Brandsdal, B. O. Molecular dynamics simulations of water and biomolecules with a Monte Carlo constant pressure algorithm. *Chem. Phys. Lett.* **384**, 288–294 (2004).
82. Darden, T., York, D. & Pedersen, L. Particle mesh Ewald: An *N*log*N* method for Ewald sums in large systems. *J. Chem. Phys.* **98**, 10089–10092 (1993).
83. Ryckaert, J. P., Ciccotti, G. & Berendsen, H. J. C. Numerical integration of the cartesian equations of motion of a system with

constraints: molecular dynamics of n-alkanes. *J. Comput. Phys.* **23**, 327–341 (1977).

84. Roe, D. R. & Cheatham, T. E. PTRAJ and CPPTRAJ: Software for processing and analysis of molecular dynamics trajectory data. *J. Chem. Theory Comput.* **9**, 3084–3095 (2013).

Acknowledgements

The synchrotron radiation experiments were performed at the BL-1A of the Photon Factory and BL45XU of the Spring-8. This work was supported in part by a Grant-in-Aid for Scientific Research from the Ministry of Education, Culture, Sports, Science and Technology, Japan (JSPS KAKENHI Grant Number JP20H00490, JP21H02636, JP22H05123, JP22H05126, JP23H00393, and JP23H02641), the New Energy and Industrial Technology Development Organization (NEDO, Grant Number JPNP20011), AMED (Grant Number JP21ak0101164 and JP24ama121027), the PRESTO program from Japan Science and Technology Agency (JPMJPR20DA), and the FORESTO program from Japan Science and Technology Agency (JPMJFR226I and JPMJFR2301).

Author contributions

T.M., T.A., and I.A. designed the experiments. Y.Z., T.M., K.S., and W.C. performed in vitro analysis and crystallization experiments. M.K. and T.T. performed MD simulations. Y.Z., T.M., T.A., and I.A. analyzed the data. Y.Z., T.M., T.A., and I.A. wrote the paper.

Competing interests

The authors declare no competing interests.

Additional information

Supplementary information The online version contains supplementary material available at https://doi.org/10.1038/s41467-024-55265-z.

Correspondence and requests for materials should be addressed to Takahiro Mori, Takayoshi Awakawa or Ikuro Abe.

Peer review information *Nature Communications* thanks Marcio Dias, Laurent Maveyraud, and the other anonymous reviewer(s) for their contribution to the peer review of this work. A peer review file is available.